Improved potential-energy and dipole-moment functions of the ground electronic state of phosphorus nitride

V. G. Ushakov[a], M. Semenov[b], S. N. Yurchenko[b], A. Yu. Ermilov[c], E. S. Medvedev[a]

[a] *Federal Research Center of Problems of Chemical Physics and Medicinal Chemistry (former Institute of Problems of Chemical Physics), Russian Academy of Sciences, 142432 Chernogolovka, Russian Federation*

[b] *University College London, United Kingdom*

[c] *M. V. Lomonosov Moscow State University, Russian Federation*

Abstract

Ab initio calculations of the PN potential and electric dipole moment in the $X^1\Sigma^+$ ground electronic state were performed at short bond lengths, $r = 0.2$–0.8 Å, and semi-empirical analytical potential-energy and dipole-moment functions were constructed based on all available experimental and theoretical information. The analytical forms for the potential-energy functions include the Extended Morse Oscillator and the Extended Hulburt-Hirshfelder potential. The dipole-moment function of PN was presented by our irregular and rational functions previously used for CO. The potential-energy and dipole-moment model functions were fitted simultaneously to the experimental line positions and permanent dipoles at v = 0-2, as well as to the *ab initio* data from our present and previous studies. With these new functions, the improved line list for the ground electronic state of $^{31}P^{14}N$ was calculated. We show that the new analytic representations of the potential and dipole moment functions help significantly reduce the numerical noise in the intensities of high overtones as well as the associated saturation at high wavenumbers leading to the so-called "overtone plateaus" in spectra of diatomic molecules (see Medvedev *et al.*, J. Mol. Spectrosc., **330**, 36 (2016)) and thus provide reliable transition intensities at very high transition frequencies. The 3-0 band is identified as vibrational anomaly, and rotational anomalies inside this and some other bands are found.

1. Introduction

The importance of PN for astrophysics was described in detail in Refs. [1, 2]. In these papers, model potential-energy and electric-dipole-moment functions (PEFs and DMFs) were constructed based on the experimental line positions and the *ab initio* calculations for the ground and several excited electronic states. It turned out that the ground-state DMFs and PEFs of PN used lead to unsatisfactory description of the intensities of high-overtone transitions, as was

recently demonstrated for several diatomics in Ref. [3], including PN. This is illustrated in Fig. 1, where the calculated intensities of the overtone transitions v-0 R(0) in the $^1\Sigma^+$ ground state of PN from Ref. [1] clearly show nonphysical saturation at $v > 6$ (circles *1*). When a polynomial function is used in the present study instead of splines to interpolate the *ab initio* DMF of Ref. [1], this saturation disappears (squares *2*), yet another one emerges at $v > 13$ caused by the discontinuity of the PEF higher derivatives at r_e (PEC-R in Ref. [1]).

In this paper, we design analytical representations for the DMFs and PEFs of PN, all without discontinuities, which lead to systematic improvement of the overtone intensities with no saturation effects up to the maximum limit achievable with the standard double precision arithmetic (triangles *3* and diamonds *4*). The remaining saturation at $v > 23$ is due to insufficient accuracy of calculation of very low overtone intensities and can be in principle further improved by using the quadruple-precision arithmetic (not shown) or by calculating an equivalent integral in the complex plane [4, Appendix] (pluses *5*); in the latter case, double and even simple precision is sufficient.

Here, we use our positive experience with the accurate calculations of the overtone-transition intensities in the ground electronic state of CO [6] to study a different diatomic molecule, PN, where we follow the approach based on the arguments presented in Ref. [4, Appendix] and references therein. A Review of these arguments can be found in Appendix A, although presented at a slightly different angle. At this junction, it should be stressed[1] that all calculations in the present paper are performed with use of the traditional method, *i.e.* by solving the Schrödinger equation and calculating the transition integral whereas the NIDL theory of Appendix A is used only as a powerful tool to analyze the numerical results.

In Sec. 2 we describe our new *ab initio* calculations aiming at extending the data toward the shorter bond lengths, and further, in Sec. 4, we explain why the data are needed in a region where the potential is millions cm^{-1} and the wave functions are strictly zero. In Sec. 3, the analytic PEFs of PN are presented, which are the Extended Morse Oscillator (EMO) and the Extended Hulburt-Hirshfelder (EHH) model; we also describe the electric dipole moment of PN with the DMFs used for CO [3, 4, 6]. In Sec. 5, basic requirements to the model PEFs and DMFs are formulated. In Sec. 6, we describe the data sets used to fit the functions and review the fitting procedure. In particular, we apply a new method in which the PEF and DMF of PN are fitted simultaneously to all the available experimental data and the *ab initio* potential and dipole moment. In Sec. 7, properties of the fitted functions are reviewed. In Sec. 8, the new calculated line list of PN and the associated spectra up to 20000 cm^{-1} are presented. Section 9 describes the anomalies in the calculated vibrational-rotational bands of PN, and estimates of the calculation uncertainties are given in Sec. 10.

[1] We are grateful to the Referee for his criticism.

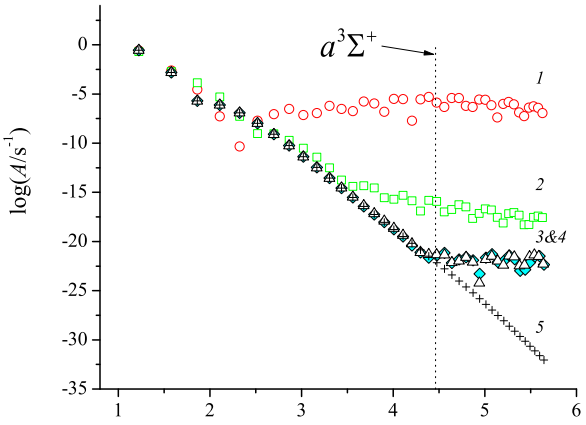

Figure 1: Einstein A coefficients of the PN v–0 R(0) overtone transitions, $v = 1$–40. *1*, data of Ref. [1], spline-interpolated DMF and empirical PEF (PEC-R) in the Extended Morse Oscillator (EMO) form with discontinuous higher derivatives at r_e; *2*, the same PEF as in *1* and the six-order polynomial DMF (present study) fitted to the same *ab initio* data as in [1]; *3*, the irregular DMF (irreg13) and the EMO PEF of the present study, all without discontinuities (see Sec. 3); *4*, the irreg13 DMF and the Extended Hulburt-Hirshfelder (EHH) PEF of the present study; *5*, the result of the calculation of the transition integral with the same PEF and DMF as in *4* along a path in the complex plane, see Appendix A. The dotted line shows the bottom of the first excited electronic state above which the model of the isolated ground state does not apply. $\omega \approx \omega_e = 1337$ cm^{-1} [5].

2. *Ab initio* calculations

Towards construction of the DMFs with extended coverage at shorter bond lengths (< 0.8 Å), new high level *ab initio* calculations were performed. Two calculation strategies were explored.

In the first one, all calculations were carried out using the coupled-cluster method CCSD(T). No electrons were included in the core. The atomic basis set cc-pV6z for both atoms was used. The DMF was calculated by the finite-field technique: The molecule is perturbed by a small electric field, $E = \pm 0.001$ a.u., along the molecule axis. The DMF was calculated by the formula $d(r) = (V(r,E) - V(r,-E)/2E)$ where $V(r,E)$ is the PEF in the presence of the electric field. Both PEF and DMF were calculated within the range of 0.2-2.5 Å. All calculations were carried out by the GAMESS-US program package [7]. The PN molecule is characterized by the closed-shell system, therefore the CCSD(T) method is expected to be reliable for the internuclear distances not too far from the equilibrium, within the range of about 0.7–2.0 Å. Still we will use the short-range data as explained in Sec. 6.

In the second method, *ab initio* calculations of the PEF and DMF in the ground electronic state of PN were performed in the far-from-equilibrium geometries at $r = 0.3$-0.7 Å using MRCI as implemented in MOLPRO 2020 [8]. The internally contracted multireference configuration interaction (icMRCI) method was used with the aug-cc-pV5Z basis set level of theory for both phosphorus and nitrogen atoms. The Douglas-Kroll correction was taken into account without the core-valence correlation for these calculations, denominated as -DK in the basis set. The complete active space self-consistent field (CASSCF) calculation was run with active space selected to be (9,3,3,0) with (4,1,1,0) as closed orbitals, similar to some of the previous work [2, 9]. The state-averaging set consisted of 11 singlet configurations ($4A_1$, $2B_1$, $2B_2$, and $3A_2$). An *ab initio* grid consisting of 10 equidistant bond lengths from 0.3 to 0.7 Å was used whereas the data points of 0.7-3.5 Å are extracted from our previously published work [2].

3. Potential-energy and dipole-moment functions

Two model PEFs are considered. One is the standard EMO potential [10],

$$V_{\rm EMO}(r) = D_{\rm e}\left[1 - e^{-\beta(r)(r-r_{\rm e})}\right]^2, \tag{1}$$

$$\beta(r) = \sum_{i=0}^{4} \beta_i \left(\frac{r^4 - r_{\rm e}^4}{r^4 + r_{\rm e}^4}\right)^i, \tag{2}$$

where β_3 and β_4 are not put to zero on the left of $r_{\rm e}$ as was done in Ref. [1]. The EMO PEF has 7 adjustable parameters.

The other one we call the Extended Hulburt-Hirschfelder (EHH) potential,

$$V_{\rm EHH}(r) = D_{\rm e}\left[\left(1 - e^{-q}\right)^2 + cq^3\left(1 + \sum_{i=1}^{3} b_i q^i\right)e^{-2q}\right], \tag{3}$$

where $q = \alpha\,(r - r_{\rm e})$. As distinct from the original Hulburt-Hirschfelder form [5, 11] (see Eqs. (9) and (15), respectively), the expansion in the second term is extended up to the third order. Cazzoli *et al.* [5] noted that the Hulburt-Hirschfelder potential was very successful in reproducing both the experimental and *ab initio* data, see [5, Fig. 1]. This was the reason to try its extended version here. The EHH PEF also has 7 adjustable parameters, including $D_{\rm e}$ and $r_{\rm e}$ in contrast to Ref. [1] where they were fixed at the values indicated in Table 4. Energies are in $\rm cm^{-1}$, r in Å.

The general mathematical structure of this model is identical to the MHH7 model recently proposed by Hajigeorgiou [12]. Both models have 7 adjustable parameters and the seemingly sole difference is the choice of the reduced internuclear coordinate. However, MHH7 is not analytic at equilibrium since it contains discontinuities in the higher derivatives, which has no effect on the energy levels, the focus of Hajigeorgiou's paper, but is not desirable for calculating the transition intensities leading to saturation as demonstrated in the present paper in Fig. 1 for the EMO model (curve *2*). The same notion relates to the previous Hajigeorgiou paper [13] where a different EHH model, yet with similar non-analytic behavior at $r_{\rm e}$ and one more point, was presented.

Our first model DMF is an irregular function with two branch points in the upper half-plane as was recommended in Ref. [4],

$$d_{\rm irreg}(r;n,k) = \frac{[1-\exp(-\alpha r)]^n}{\sqrt{\left(r^2-a_1^2\right)^2+b_1^2}\sqrt{\left(r^2-a_2^2\right)^2+b_2^2}} \sum_{i=0}^{k} c_i \left(1-2e^{-\beta r}\right)^i . \quad (4)$$

It depends on $7+k$ variable parameters.

According to theory [14], the asymptote at the united-atom (UA) limit depends on the UA electronic configuration. In our case, the UA is ^{22}Ti with the $^3\rm F_2$ ground state [15], therefore DMF $\propto r^5$. The asymptote at infinity is r^{-4} if at least one atom has quadrupole moment. In the present case, both P and N have quadrupole moments due to the electrons at the p-orbitals with the ^{14}N value given in [5, Table 1] and [16, Table II]. The DMF in Eq. (4) satisfies this requirement at infinity. In Eq. (4), we used the theoretically justified value of $n = 5$ (UA value) and the value of $n = 3$ for the function that will be used for comparison.

Functions $d_{\rm irreg}(r;5,4)$, $d_{\rm irreg}(r;5,5)$, and $d_{\rm irreg}(r;5,6)$ will be called irreg11, irreg12, and irreg13 DMFs, respectively. We will show that irreg13 is our best DMF, the others will be used for comparison. Function $d_{\rm irreg}(r;3,4)$ leads to intensities with "incorrect" behavior, therefore it will be called the wrong DMF.

Two additional DMFs based on the rational form,

$$d_{\rm rat}(r) = \frac{ar^3}{\Pi_{i=1}^4\left[(r-r_i)^2+v_i^2\right]}, \quad (5)$$

will be used for comparisons. This form contains 9 adjustable parameters. The DMFs are in debye.

All the above functional forms for the PEF and DMF contain adjustable parameters that are determined by minimization of the difference between the calculated and input data characterized by χ^2, Eq. (6), which is a measure of the quality of the fit. The input five data sets and the details of the minimization procedure are described in Sec. 6. For the rational form of Eq. (5), two local minima of χ^2 with nearly the same values of χ^2 were found that gave two sets of parameters. The corresponding rational DMFs will be called ratA and ratB.

4. Why we use the very short bond lengths values

As we showed earlier [17], in order to improve the numerical stability of the overtone intensities, it is important to use analytic functions with adjustable parameters to represent model PEFs and DMFs, which are rather rigid constructions. If we add new *ab initio* data at 0.2–0.8 Å, we have to refit the functions, which then change everywhere including the classical region between the turning points where the contribution to the transition integral comes from. The resulting relatively small changes of the wave functions and DMF in the region of integration will have large impact on the high-overtone transition probabilities, which are exponentially small due to severe cancellation of the $\pm$ contributions of the integrand.

5. Requirements for the model dipole moment and potential energy functions

A powerful tool to analyze the intensities of the vibrational overtone transitions is the Normal Intensity Distribution Law (NIDL) that was derived theoretically and verified experimentally as described in review [18] and references therein. According to the NIDL, the transition-dipole-moment values of the overtone transitions are expected to decay exponentially. The NIDL-like behavior of the transition probabilities in the form of Einstein A coefficients of PN is illustrated in Fig. 1, where the values of $\log(A)$ for high-enough overtones show linear dependence when plotted against $\sqrt{E_v/\omega}$ used as an overtone count (E_v is the vibrational energy and ω is the harmonic frequency). The perfect NIDL up to A as low as 10^{-32} s^{-1} seen in Fig. 1 tells us about the unprecedentedly high quality of the molecular functions.

As discussed in [17], it is important to represent the potential energy and the dipole moment as analytic functions of r in order to avoid the numerical noise caused by extrapolations from any grid-based representations using splines or piece-wise smooth functions. The analytic representations of the PEFs and DMFs are built in our previous [6] and present papers by fitting the associated adjustable parameters to the corresponding *ab initio* values and the experiment, *i.e.*, line positions (or energies), the permanent dipoles, and the intensities (or transition dipole moments).

Before entering the details of the fitting procedures, let us formulate the necessary requirements that the analytic representations of PEFs and DMFs

must obey. As explained in Appendix A, the fitted PEF and DMF can be "correct" or "wrong" depending on their analytic properties in the complex plane (*i.e.*, when the bond lengths values are extended to the complex numbers), where any analytic function unavoidably has singularities like poles and branch points. They can also oscillate or increase in the complex plane. All these features can in principle contribute to the intensities of overtone transitions, but only the pole at $r = 0$, or more precisely the repulsive branch of the potential associated with it has physical meaning.[2] Therefore, the necessary requirements for such analytic funcitons are: 1) all other singularities (except $r = 0$) must not overweight the contribution from the repulsive part of the potential, or, equivalently, they should not be located very close to the classical region; for PN, this is about 1 bohr; 2) the functions should not increase or oscillate in the upper half of the complex plane. With these restrictions fulfilled, the model functions will provide the exponential fall-off of the intensities required to manifest in the form of the NIDL, *i.e.*, a straight-line distribution like that shown in Fig. 1. As mentioned above, the non-analytic functions like splines and piece-wise smooth functions result in a power-like law or even saturation having nothing to do with the physical intensities; the analytic functions violating rules 1 and 2 above result in a wavy intensity distribution like squares in Fig. 4 declining from the NIDL, that also greatly overestimate the intensities.

Let us consider our models from this point of view. The EMO potential in Eq. (1) has poles in the complex plane, one of them at $r = r_e e^{i\pi/4}$, but, as shown by curve *3* in Fig. 1, they do not degrade the NIDL because they are located far from the real axis. The same is true for the potential of CO by Meshkov *et al.* [6], which also has poles far from the real axis.

On the contrary, the DMFs in Eqs. (4) and (5) have branch points and poles, which can affect the intensity distribution strongly thereby destroying the NIDL. We will show in the next section how to avoid this undesirable effect by proper adjusting the DMF parameters. As a result, the fitted irreg13 DMF does not spoil the NIDL as seen in Fig. 1, curves *3* and *4*.

6. The fitting procedure

For determining the parameters of the model potential and dipole functions, the following sets of data are used: 1) the experimental transition frequencies, as in Ref. [1], collected from Refs. [5, 16, 19–21], $v \leq 11$; 2) the experimental permanent dipole moment (PDM) values at v = 0,1,2 [22, 23]; 3) the *ab initio* potential PEC-A and the dipole moment function from Ref. [1] in the range of 1.5-10 a.u.; 4) the *ab initio* potentials of Ref. [2] (all methods) and of the present study; 5) the dipole moment values at $r < 0.8$ Å of the present study.

The reason to separate the short-range DMF data stems in the fact that they are highly unreliable, yet bearing important information on the sign change of

[2]The Morse potential has no pole at $r = 0$, yet its repulsive branch provides the intensity distribution in the form of the straight NIDL line.

the PN DMF as manifested by the results of two independent methods shown in Fig. 2 by circles and crosses. Therefore, our task is to use set 5 in such a way as to preserve the DMF sign change without deteriorating the NIDL conditions, which could easily occur if the branch points of the irregular DMF came close to the real axis where the main contribution to the transition dipole moment (TDM) integral, $\langle v''J''|d(r)|v'J'\rangle$, comes from or by other reasons specified in Sec. 5. Here $|v'J'\rangle$ is rovibrational eigenfunction. This task can be performed by assigning large enough individual uncertainties used as inverse weights in the fitting procedure to the *ab initio* points of set 5.

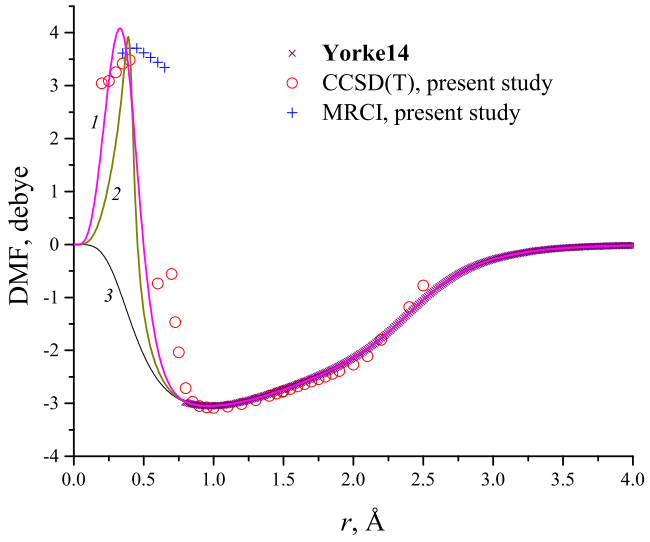

Figure 2: The *ab initio* (points) and fitted (lines) DMFs. *1*, irreg13; *2*, irreg12; *3*, irreg11.

The least-squares fitting was performed by minimization of the following functional:

$$\chi^2 = \sum_{\alpha=1}^{5} \chi^2_\alpha, \tag{6}$$

$$\chi^2_\alpha = \sum_i \left(\frac{y^{\rm fit}_{\alpha i} - y^{\rm dat}_{\alpha i}}{\sigma_{\alpha i}} \right)^2, \tag{7}$$

where y's are transition frequencies, PDMs, *ab initio* PEF and DMF points, and χ^2_α are contributions of the individual data sets. We also will discuss the total reduced and individual standard deviations,

$$\chi_{\rm red} = \sqrt{\chi^2/N},\ {\rm std} = \sqrt{\frac{1}{N_\alpha} \sum_i \left(y^{\rm fit}_{\alpha i} - y^{\rm dat}_{\alpha i} \right)^2}, \tag{8}$$

where N and N_α are the total and individual numbers of the data points.

Initially, we followed Ref. [1] by fitting the irreg11 DMF only to set 3. Since the short-range data were not used in the fitting, curve *3* in Fig. 2 remained negative everywhere. Two other DMFs, irreg12 and irreg13, shown in the figure were fitted to all five data sets simultaneously with the EHH PEF, see the next paragraph. Curves *1* and *2* poorly reproduce the *ab initio* points at $r < 0.8$ Å because of large uncertainties, yet they do change sign as required.

In this paper, for the first time to the best of our knowledge, we perform simultaneous fitting of the PEF and DMF to all available experimental and theoretical data. This means that the functional in Eq. (6) has contributions from both the potential and dipole-moment data. The necessity in such kind of fitting stems in the fact that there are high-precision data on the PDM of PN at $v = 0$–2, which depend on both the PEF and DMF. There exist no experimental data on the transition intensities bearing information on the DMF. Therefore set $\alpha = 2$ of the PDMs proved to be very important since it restricted the parameters very strongly due to high precision of the data. Similarly, the experimental frequencies of set 1 are very important because, in combination with set 2, they guarantee the correct r_e value very close to experiment, see Table 4. Further discussion of this issue is given in Sec. 7.

Apart from the requirements formulated in Sec. 5, which the fitting procedure must fulfill, another important problem is assigning uncertainties to the *ab initio* data, which are not known. We gave $\sigma_{\alpha i} = 5\%$ to all *ab initio* potential energy data since this is a typical scatter of the values obtained with different methods and different basis sets. This choice is also justified by the fitted values of D_e and r_e for the EHH potential shown in Tables 2 and 4 that are very close to their experimental values. For the EMO potential, the value of $D_\mathrm{e} = 53388$ cm^{-1} obtained (see Table 1) is worse than that obtained with the EHH PEF, therefore we consider EHH as the best PEF to be used for calculation of the line list.

The *ab initio* DMFs at $r > 0.8$ Å were assigned uncertainties of $\sigma_{\alpha i} = 0.02$ debye, which is a typical scatter obtained with different methods. The data at $r < 0.8$ Å were individually assigned with large uncertainties varying from 0.5 to 20 debye in order to fulfil, first, the requirement of the sign change and, second, the restrictions of Sec. 5 on the DMF properties in the complex plane.

Minimization of the functional in Eq. (6) has been carried out by a home-made program using the Levenberg-Marquardt method. The level energies and the corresponding wave functions have been calculated by the sinc-DVR method applied to the Schrödinger equation transformed by the variable substitution $y = (r^2 - r_0^2)/(r^2 + r_0^2))$, $r_0 = 1.49$ Å. This procedure is in line with the adaptive analytical mapping approach of Meshkov *et al.* [24]. The Einstein A coefficients (in s^{-1}) were calculated by the formula

$$A = 3.1361887 \times 10^{-7} \tilde{\nu}^3 \frac{\mathrm{HL}}{2J'+1} |\mathrm{TDM}|^2, \qquad (9)$$

where $\mathrm{HL} \equiv |m|$ is the Hönl-London factor equal to $J'+1$ for the P-branch and J' for the R-branch, $\tilde{\nu}$ is transition frequency in cm^{-1} and $\mathrm{TDM} = \langle v''J''|d(r)|v'J'\rangle$

is transition dipole moment in debye.

Table 1: Fitted parameters of the EMO PEF

D_e, cm^{-1}	0.5338810940280822E+05
r_e, Å	0.1490865783006148E+01
β_0, $Å^{-1}$	0.2188250046485733E+01
β_1, $Å^{-1}$	0.1467040829582623E+00
β_2, $Å^{-1}$	0.1532382369985083E+00
β_3, $Å^{-1}$	0.1376729138537458E+00
β_4, $Å^{-1}$	0.1388912048059677E+00

Table 2: Fitted parameters of the EHH PEF

D_e, cm^{-1}	0.519274276353915047E+05
r_e, Å	0.149086580348419329E+01
α, $Å^{-1}$	0.221879954515301936E+01
c	0.948616297258670499E−01
b_1	0.100084121923090996E+01
b_2	0.470612349534084318E+00
b_3	0.890787339171956738E−01

The values of the fitted parameters of the EMO and EHH potentials and the irreg13 DMF are given in Tables 1, 2, 3, and in the supplementary FORTRAN file. Table 4 shows the EHH spectroscopic parameters and compares them with the literature data. The comparison demonstrates the high quality of the EHH potential, which provides for the parameters close to their values from other sources. The fitted functions will be discussed in the next section, here a short comment is in order. If we use parameters a_i of the Dunham potential, Eq. (3) in Ref. [5], in order to derive coefficients c and b (b_1 in our Eq. (3)) in Eqs. (16) and (17) of Ref. [11][3], then inserting the a_i values from [5, Table 3] gives $c \approx 0.09455, b \approx 1.02$, which agrees with our values, $c \approx 0.09486, b_1 \approx 1.00$, as expected. However, with these Dunham potential parameters, the values of ω_e and $\omega_e x_e$ turn out to differ from the experimental ones by more than the experimental uncertainties shown in [5, Table 3] .

7. Properties of the fitted model functions

Two our model PEFs, EHH and EMO, along with PEC-R of the previous study [1] are graphically shown in Fig. 3. On the given scale, they all are

[3]There are sign misprints in the corresponding Eq. (11) of Ref. [5] ($-7/12$) and Eq. (17) of Ref. [11] ($-[...]$).

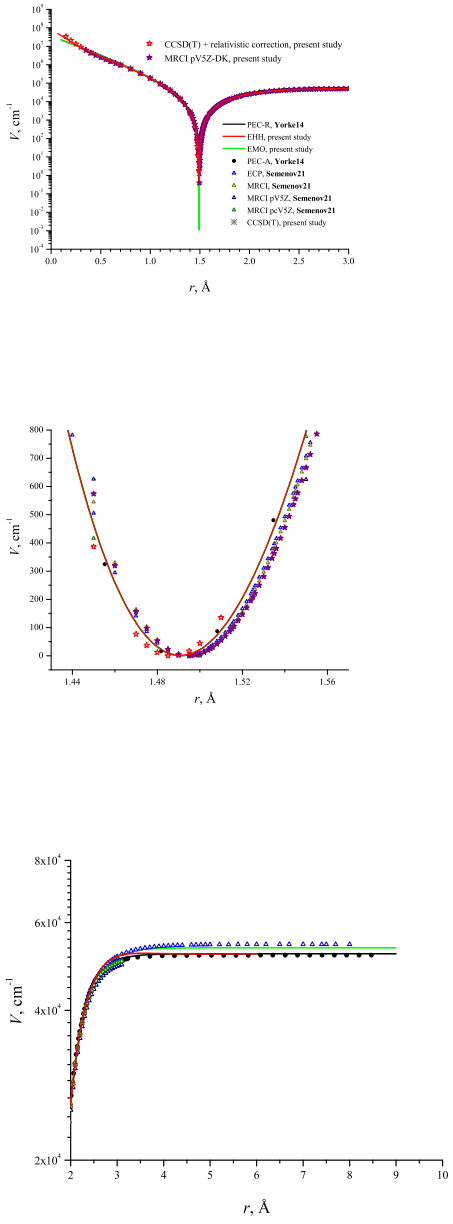

Figure 3: The *ab initio* (points) and fitted (lines) potentials of the previous [1, 2] and present studies.

Table 3: Fitted parameters of the irreg13 DMF

n	5
α, Å^{-1}	0.528882306544608771E+00
β, Å^{-1}	0.174842312392832677E+01
a_1, Å	0.367394402167278311E+00
b_1, Å	0.126545114816554061E+00
a_2, Å	0.226658916500257268E+01
b_2, Å	0.263188285464316518E+01
c_0, debye·Å^4	0.954686180104024606E+04
c_1, debye·Å^4	−0.100829376358086127E+06
c_2, debye·Å^4	0.343009094395974884E+06
c_3, debye·Å^4	−0.593296257373294560E+06
c_4, debye·Å^4	0.574050119444558513E+06
c_5, debye·Å^4	−0.296914092409155215E+06
c_6, debye·Å^4	0.644340312384712088E+05

indistinguishable over the entire range of r except for very short r where the EHH potential follows the *ab initio* points more closely than the EMO and PEC-R do. This difference is not expected to affect the intensities strongly except for very high overtones. Our EMO does not decline appreciably from PEC-R anywhere.

Near equilibrium, significant differences between the fitted potentials and *ab initio* data are seen. The very high precision of the measured permanent dipole at $v = 0, 1, 2$ and detailed dependence of the line positions upon J impose very rigid restrictions on r_e. The B_e and r_e resulting from fitting are nearly independent of the model and of the sets of the *ab initio* data, and both constants are very close to their experimental values within rather small experimental uncertainties, see Table 4. As seen in Fig. 3, r_e of *ab initio* is shifted by about 0.004 Å, which obviously corresponds to the precision of determination of r_e in the *ab initio* calculations. It is seen that the models would coincide with the *ab initio* points be the latter shifted by 0.004 Å along abscissa.

As seen from Table 5, our EMO and EHH potentials are equivalent in reproducing the line positions and do this much better than the empirical PEF of Ref. [1]. Comparing the EHH and EMO models, we see that EHH better reproduces the short-r *ab initio* data and has D_e closer to the experimental value (see Table 4). Therefore, we consider EHH as the best PEF to be used for calculation of the line list. It should be emphasized that the fitting procedure does not permit determination of the "true" dissociation limit because the available data are insufficient; rather, the fitted D_e characterizes the quality of the fitted function.

The above considerations suggest that the EHH model is slightly better than the EMO one, yet the latter can be used as a comparison function to estimate the expected uncertainties in the calculated intensities.

Table 4: The spectroscopic parameters of the EHH potential in comparison with the literature data

parameter	value	reference
D_e	51940 cm^{-1}	**Yorke14** [1]
	51927 cm^{-1}	This work
ω_e	1335.6(15) cm^{-1}	**Wyse72** [16]
	1337.0(1) cm^{-1}	**Ghosh81** [20]
	1336.99230(66) cm^{-1}	**Maki81** [19]
	1336.9992(52) cm^{-1}	**Cazzoli06** [5]
	1336.9972 cm^{-1}	This work[a]
$\omega_e x_e$	6.5(5) cm^{-1}	**Wyse72** [16]
	6.88(2) cm^{-1}	**Ghosh81** [20]
	6.91192(40) cm^{-1}	**Maki81** [19]
	6.9164(34) cm^{-1}	**Cazzoli06** [5]
	6.9134 cm^{-1}	This work[a]
r_e	1.4908696082 Å	**Yorke14** [1]
	1.49086(2) Å	**Wyse72** [16]
	1.490865803 Å	This work
$B_{v=0}$	0.7837138(87) cm^{-1}	**Ahmad95** [21]
	0.78371339 cm^{-1}	This work[b]
	0.78371551(22) cm^{-1}	**Ahmad95** [21]
	0.7837156(7) cm^{-1}	**Ghosh81** [20]
	0.78371557 cm^{-1}	This work[c]
B_e	0.7864888(27) cm^{-1}	**Wyse72** [16]
	0.78648563(20) cm^{-1}	**Maki81** [19]
	0.786486(4) cm^{-1}	**Ghosh81** [20]
	0.7864844(28) cm^{-1}	**Ahmad95** [21]
	0.78648611(12) cm^{-1}	**Cazzoli06** [5]
	0.786485916 cm^{-1}	This work[d]

[a] From the potential derivatives [25].
[b] One half of the $J = 1 \rightarrow 0$ transition frequency at $v = 0$.
[c] Average of $\hbar^2/2\mu r^2$ over the $v = 0$ state.
[d] $\hbar^2/2\mu r_e^2$.

Table 5: The individual standard deviations of the transition frequencies (cm^{-1}) and the total reduced standard deviation of the fits

PEF	std 1	std 2	std 3	χ_{red}
PEC-R of **Yorke14** [1]	7.9e-5	4.0e-3	9.2e-2	67
EMO (present study)	1.2e-6	7.7e-4	4.3e-2	1.4
EHH (present study)	1.3e-6	9.0e-4	4.7e-2	1.5

std 1, purely rotational transitions (24 lines)
std 2, all transitions excluding **Ghosh81** [20] data (111 lines)
std 3, all data (122 lines)

Now let us discuss the properties of the fitted DMFs. The irreg13 DMF is considered as the best model function for PN. In the following, arguments are presented in support of this statement.

Figure 4 shows the vibrational Einstein A coefficients for the v-0 R(0) transitions of PN calculated with the PEF EHH and three DMFs including irreg13 and two comparison DMFs: a six-order polynomial (poly6, fitted only to the r = 0.8–2.2 Å *ab initio* data) serving as a reference and the other one called "wrong" DMF. Based on these plots, one can judge whether they obey the NIDL or not.

The irreg13 DMF gives a very straight NIDL-like drop-off of the transition intensities, Eq. (9), nearly identical at high v to that of poly6. Such a coincidence cannot be accidental, it testifies that the two DMFs with such different analytic properties and, moreover, fitted to different data sets approach one and the same true molecular function. This situation agrees with our intuitive expectation that the intensities must be insensitive to the difference in analytic representations of DMF under the condition that they are "correct", see Appendix A. The rational form of Eq. (5) gives a bit larger differences with poly6 (not shown), yet it will be used to give a rough estimate of the uncertainties of the calculated intensities.

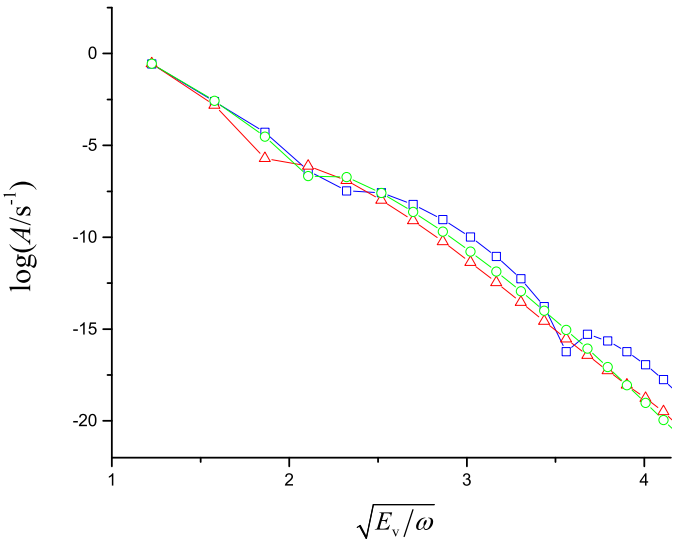

Figure 4: The intensities of v-0 R(0) lines generated by the EHH potential and three DMFs. Circles, poly6 as a reference to compare with; triangles, irreg13 (the same as in Fig. 1); squares, wrong DMF.

In contrast, the third function classified as wrong results in the wavy dependence of the overtone transition probability declining from the NIDL, hence

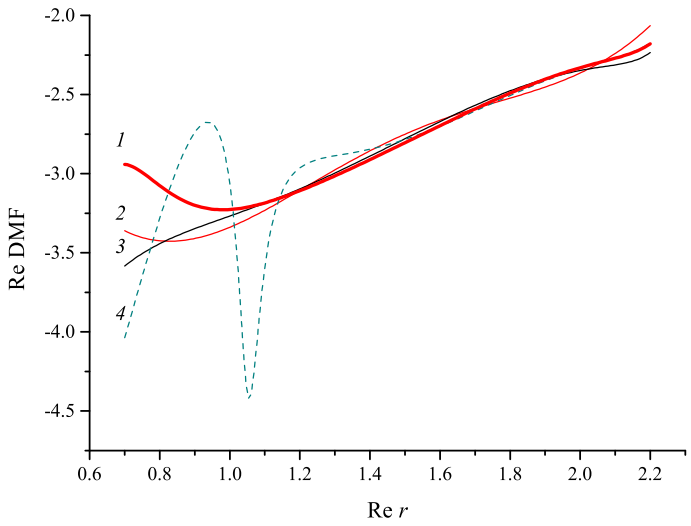

Figure 5: The real part of the DMFs along the line $\mathrm{Re}(r) + 0.4i$ parallel to the real axis. *1*, irreg13, the best DMF; *2*, poly6; *3*, irreg11; *4*, the wrong DMF.

the intensities differ very strongly from both the reference poly6 and the irreg13 DMFs. This is the reason to consider this DMF unsatisfactory. Analysis below shows that the wrong DMF breaks one of the necessary conditions for the "correct" behavior formulated in Sec. 5. Since such a behavior is characteristic of the particular model rather than the true molecular function, this DMF must be rejected.

Let us make a useful note that in practice the given DMF form can be tested without tedious calculations of the intensities and plotting them in the NIDL coordinates. Namely, the requirement of smooth behavior in the complex plane formulated in Sec. 5 can be immediately verified as soon as the analytic form with the fitted parameters is known. In Fig. 5, the real parts of four DMFs are plotted along the line parallel to the real axis and shifted up by 0.4 Å. Curves *1-3* show smooth behavior whereas curve *4* makes a large-amplitude oscillation, which undoubtedly indicates the defectiveness of this function.

8. The line list and the absorption spectrum of ^{31}P^{14}N

As part of this work, the line list for ^{31}P^{14}N in its $X\,^1\Sigma^+$ ground electronic state was calculated with the EHH PEF and the irreg13 DMF using the Duo program [26], a free-access rovibronic solver for diatomic molecules available at https://github.com/exomol/Duo/. These functions, EHH and irreg13, have been implemented in Duo as part of the Duo library of functional

forms. The spectroscopic model of PN used is given in the Supplementary material as the Duo input file. The wavenumber range in the line list is from 0 to 51974 cm^{-1}, $J \leq 270$. Both the lower and upper state thresholds were mapped to 51927 cm^{-1}, which is approximately the dissociation threshold for the ground electronic state. The line list contains 254597 transitions between 9590 vibrational-rotational states. The line list will be available via the ExoMol website.

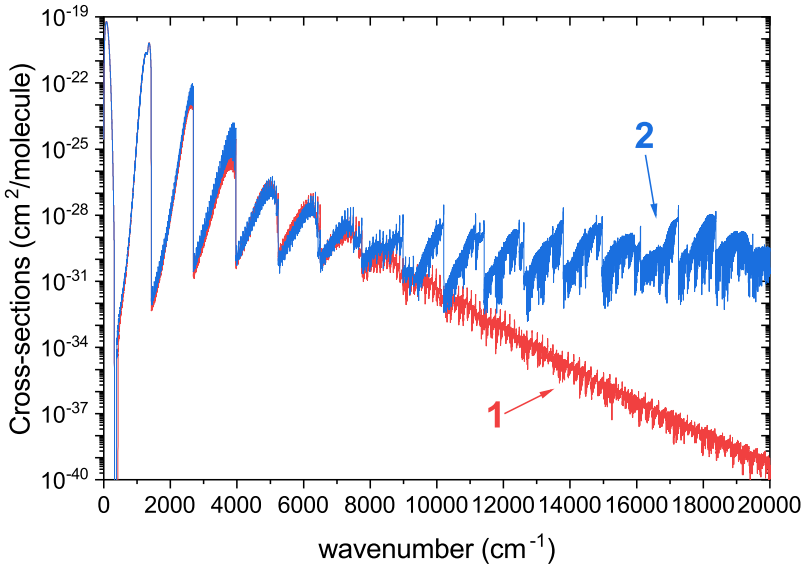

Figure 6: The calculated absorption spectrum of ^{31}P^{14}N at 2000 K well below the bottom of the first excited electronic state. *1*, present study; *2*, previous study [2]

The Einstein A coefficients produced as part of the line list were then used to calculate the absorption spectrum of PN for the ground state and to compare it to our previous work. In Fig. 6, we can see the comparison of the vibrational-rotational spectra due to the X-X transitions calculated in this work and in the previous work by Semenov *et al.* [2]. The absorption spectrum is calculated at 2000 K with the Gaussian line profile of HWHM = 1 cm^{-1}. It is seen that the new DMF provides a significant improvement in the structure of the spectrum. Especially large changes are observed above 7000 cm^{-1} due to removal of the nonphysical saturation of the high-overtone transitions caused by the spline-interpolated DMF.

Less dramatic, yet significant are changes in the IR region below 7000 cm^{-1} that are better visible in the stick spectrum of Fig. 7.

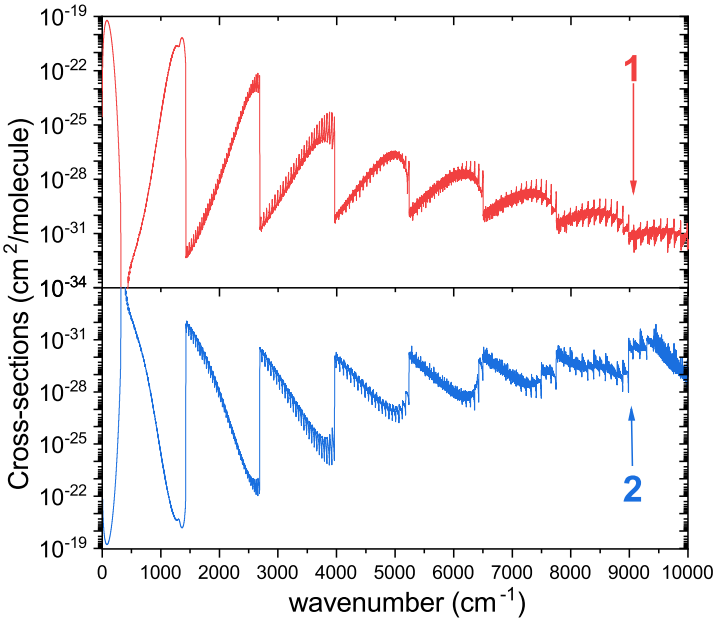

Figure 7: The low-frequency part of the spectrum of Fig. 6. *1*, present study; *2*, previous study [2].

9. Vibrational and rotational anomalies

Anomalies are very common phenomenon in the calculated line lists of diatomic molecules, and some of them were observed in experiment. They were predicted, for the first time, by Le Roy and coworkers [27, 28] in the electronic transitions of I_2. It was discovered that the Franck-Condon amplitude (the radial overlap integral) as function of J crosses zero and changes sign at some J, thereby weakening the intensities of the neighboring lines. Such kind of anomalies are present in the H_2 line list [29] calculated recently by Abgrall *et al.* [30].

The anomalies in the X-X vibrational transitions were described in Ref. [18]. They arise when the TDM as function of Δv crosses zero and changes its sign[4], thereby making the intensities of the neighboring bands very weak as compared to the values predicted by the NIDL. The vibrational anomalies were predicted in HF [31], predicted and observed in CO [32, 33]. Here in Fig. 4, the PN 3–0 band is such a vibrational anomaly calculated with the best PEF and DMF of the present study (triangles); it is seen in Fig. 1 as well.

[4]The signs of TDMs depend on the choice of signs of the vibrational wave functions [18]. Here, we choose the signs by imposing the condition that the wave functions were positive at $r \to 0$. Under this condition and in the absence of the anomalies, the signs of TDMs do not change in the sequence of v-0 transitions, see Appendix A, Eq. A.14.

Table 6: The TDM values (debye) for the v–0 R(0) lines

v	TDM
1	−3.4E-02
2	−9.0E-04
3	−1.8E-05
4	7.2E-06
5	2.1E-06
6	4.7E-07
7	1.0E-07
8	2.3E-08
9	5.3E-09
10	1.3E-09

An additional proof that the 3-0 band is an anomaly is presented in Table 6 and Fig. A.11 based on the well-known regularities of the sign changes in the successive v–0 transitions [18, 34, 35]. It is seen that the TDM changes sign between $v = 3$ and 4.

The 3-0 anomaly is not very deep, as is evident in Fig. 1. It is not seen in the spectrum of Figs. 6 and 7 because there are a lot of transitions at 2000 K superimposing on it. However, it is very sensitive to the analytic form of DMF, which is manifested in Figs. 1 and 9, therefore it can be useful, if observed in a linear spectrum, for refining the molecular functions.

Finally, the rotational anomalies in the vibrational bands due to sign change of the TDM as function of J are also met very often [36]. In particular, lines P(17) and P(18) of the PN 3-0 band shown in Fig. 8 is a rotational anomaly inside the vibrational anomaly 3-0. Table 7 lists several anomalies with the highest values of A. Supplementary material contains the rotational distributions within several PN bands with anomalies.

The anomalies are interesting because their intensities are very sensitive to the form of the molecular functions, both potential and dipole [37]. Therefore, when observed, they could help significantly improve the molecular functions. In Table 7 we collected some anomalies with the highest values of A. It is still unclear whether such anomalies can be observed in PN because even the intensities of the PN fundamental transitions with $A \approx 1$ s^{-1} have not been measured yet. In the case of H_2, the observed normal lines in the $\Delta v = 1, 2$ emission bands have the A values on the order of 10^{-7} s^{-1} [38, Table 1]. In the case of the CH^+ ion, the anomalous 1–0 R(7) transition in emission was observed with $A = 0.001$ s^{-1} [39, Table B2].

10. Discussion and conclusions

We constructed the new PEF that reproduces the known PN spectroscopic parameters very well, as can be seen in Tables 4 and 5. We also constructed

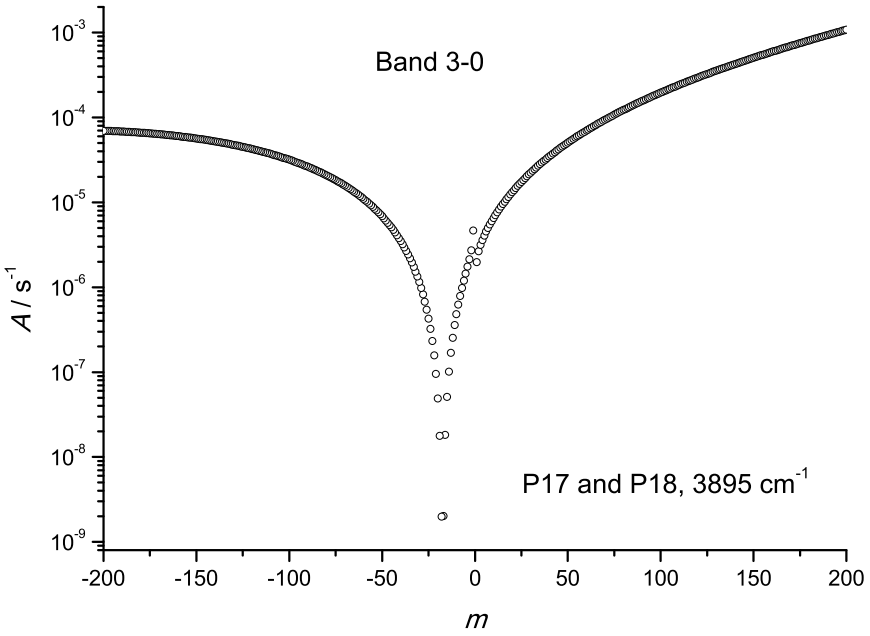

Figure 8: The rotational distribution within the 3-0 band.

Table 7: Examples of the rotational anomalies in the PN vibrational bands. More anomalies and the rotational distributions within the bands with anomalies are given in Supplementary material

Δv	line	ν, cm^{-1}	A, s^{-1}
2	2-0P(93)	2395	3e-8
	3-1P(94)	2364	5e-10
3	3-0P(18)	3895	2e-9
	4-1P(21)	3847	5e-9
4	9-5R(41)	4952	2e-9
	14-10R(25)	4667	6e-8
	16-12R(19)	4550	1e-7
5	10-5R(92)	6014	1e-9
	15-10R(79)	5695	2e-8
6	20-14R(103)	6275	1e-8
7	20-13R(134)	7062	2e-10

the new DMF, which results in a NIDL-like behaviour of the overtone transition intensities of PN.

A few comparison functions were also developed in order to estimate the expected errors in the intensity calculations. Shown in Fig. 9 are ratios of the intensities calculated with various DMFs of PN to the ones calculated with our best DMF irreg13. It is remarkable that the variations of A between five comparison functions are within one order of magnitude at v = 6-20 where A varies by 10 orders of magnitude. It is important that such relatively small variations of the predicted high-overtone intensities are made with the dipole-moment functions built upon three absolutely different analytic forms - a polynomial, an irregular function with branch points/no poles, and a rational function with poles/no branch points, which testifies that all these DMFs approach one and the same true molecular dipole-moment function. Unfortunately, there are no experimental data on the line intensities of PN in order to make the DMF more reliable.

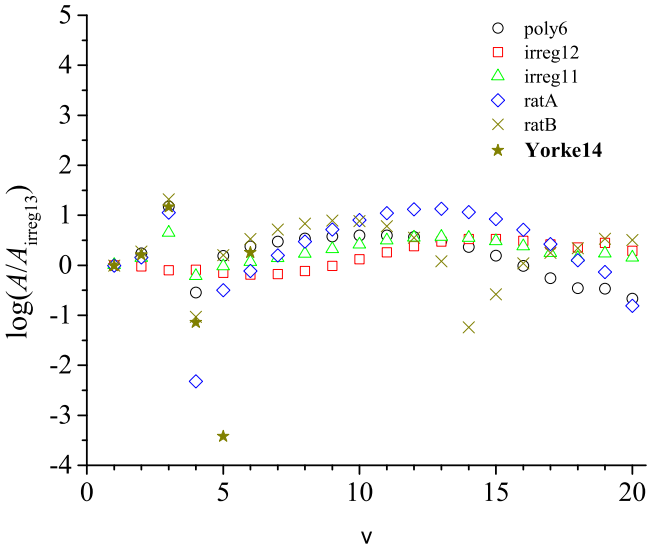

Figure 9: Ratios of the Einstein A coefficients for v–0 R(0) lines calculated with the EHH potential and various comparison DMFs, as well as those from Ref. [1], to the ones calculated with the best irreg13 DMF. The **Yorke14** data at $v > 6$ are not shown because of the saturation seen in Fig. 1.

The v–0 overtone transitions at v = 1–6 deserve special attention. Obviously, there exists an anomaly due to sign change of the transition dipole moment [36] between $v = 3$ and 4. As we know, such anomalies are very sensitive to the PEF and DMF forms [37], therefore the variations of A between different forms are very large for these bands. This feature gives a hope that the molecular func-

tions can be essentially improved when the intensities of the lines belonging to these bands will be measured. This notion relates to perspective in future since at present even the intensities in the rotational band and in the fundamental vibrational band have not been measured yet.

Acknowledgements

The work by VGU and ESM was carried out in accordance with the state task, state registration number AAAA-A19-119071190017-7. The work of SY was supported by the European Research Council under Advanced Investigator Project 883830.

Supplementary material

File **X_PN_PEF_DMF.f**. The FORTRAN code to calculate the EHH PEF and the irreg13 DMF.

File **All X1Sigma+ PEC and dipoles.xlsx**. *Ab initio* data of **Semenov21**.

File **PN_aug-cc-pV5Z-DK_DMF_PEF_X_.xlsx**. *Ab initio* data of the present study.

File **PN_CCSD(T)_cc-pV6z_nocore.xlsx**. *Ab initio* data of the present study.

File **Examples of rotational anomalies in PN vibrational bands**. Rotational distributions in some bands with anomalies.

File **Fit_OUT_13param_obs-calc**. Comparison of the experimental and *ab initio* data with the calculations in the present study.

File **PN_EHH_irreg13.inp**. A Duo input file containing the spectroscopic model of PN used to produce the line list.

Note added in proof.

The Referee noted that the NIDL theory was developed for the X-X transitions within an isolated X state and questioned its applicability because of contributions from the excited states. Indeed, if there is a low-lying electronic excited state, the exponential falloff of the intensities is broken down and the NIDL is not obeyed at the transition energies overlapping the gap of ΔE between the ground and the first excited state. As an example, we mention CN where $\Delta E = 9247$ cm^{-1} [40] so that the upper states in the X-X transitions have significant contributions from the excited state at the transition energies greater than ΔE. As a result, the transition intensities become increasing at such energies (L. K. McKemmish, private communication). For transition energies below ΔE, the effect of the excited states is described by small modifications of the PEF and the effective masses, which does not destroy the single-state model, hence the NIDL applies.

Appendix A. Qualitative considerations of the rovibrational X-X transitions

We start with the same trivial statement as in Ref. [4].

(i) All the input experimental and theoretical information necessary to construct the molecular functions responsible for the line positions and transition intensities is of point-wise nature, hence, some interpolation scheme is needed to calculate the observables.

(ii) If it goes about the intensities within the 1–0 fundamental band, the task is very simple. Since the TDM integral is of the same order of magnitude as its integrand times a characteristic width of the integration interval, Δr, any interpolation method can be used, including linear interpolation, Simpson parabolic scheme, cubic splines, analytic functions, and any other sort of the interpolating functions; in any case, the *absolute error* in the calculated integral, $\langle v''J''|d(r)|v'J'\rangle$, arising due to the difference between the model and true functions will be of the same order of magnitude as the error in the integrand. For instance, if the integrand is on the order of unity and its error is ± 0.05, then the integral will have the same error of ± 0.05 assuming Δr on the order of unity as well.

(iii) With the overtones, the situation changes dramatically. Even the first overtone, the 2–0 band, of a molecule with no light atom (e.g., CO or PN) is 100 times weaker than the fundamental band, and the higher ones rapidly drop down with the overtone number. This means that the transition integral is orders of magnitude smaller than its integrand due to"fine cancellation" of the $+/-$ contributions caused by the oscillating wave function of the upper state; as a result, the entire integral representing the needed TDM can be much smaller than the above 5% *absolute error*. In our example, the TDM drops down by a factor of 10, hence, the *relative error* increases from 5% to 50%, making the calculation for higher overtones senseless.

(iv) **The fine cancellation for high overtones occurs only when the integrand including both the wave functions and the DMF is analytic function**, this is the first key point! To be more specific, the cancellation by 2–3 orders of magnitude for the first and second overtones still occurs with non-analytic functions, but this "coherency" is rapidly destroyed with increasing the overtone number, so that the cancellation by many orders of magnitude for higher overtones can take place only with analytic functions, and this leads to simultaneous cancellation of the above *absolute* difference of 5%. As a result, the *relative error* remains 5% for higher overtones as well. In particular, if some small corrections to the potential are introduced, say, caused by interactions with the excited electronic states (see footnote 1) or other reasons, the changes in the intensities will also be small. The non-analytic functions do not possess such high coherency, therefore the relative error in the TDM increases with the overtone number.

(v) In order to solve the problem formulated in (iii), we proposed, based on (iv) and following Landau and Lifshitz [25], to use for interpolation only the analytic functions, so much the more that the intrinsic PEF and DMF are

actually analytic over the entire complex plane of the interatomic distance r, and so must do their model representations. Indeed, neither the Hamiltonian and dipole-moment operators, nor the Schrödinger equation contain terms with discontinuous derivatives.

(vi) The second key point: Under some additional restrictions (see point (ix) below), which are always fulfilled in real molecules, **the intensities of the overtone transitions calculated with analytic PEF and DMF are exponentially decreasing with increasing the overtone number**. The proof follows from the unique properties of the analytic functions and the Landau method to calculate small transition probabilities [25].

We remind that the analytic functions, by definition, are continuous with all their derivatives at any value of the complex variable r except for singularities like poles and branch points. The great advantage of such functions over splines and other functions with discontinuous derivatives stems in three strict theorems: 1) any analytic function can be extended from the real axis into the complex plane in a unique fashion, which permits using powerful methods unavailable for non-analytic functions; 2) the integration path C can be shifted, without changing the integral, from the real half-axis, $r = 0 - \infty$, into the complex plane keeping the end point $r = 0$ fixed, which can be used to decrease the integrand to the level of the whole integral under condition that the integrand does not increase in the upper half-plane; and 3) if path C is shifted in the upper half-plane as proposed in theorem 2 above, the dominant contribution to the integral along the new path C comes from either one of the singular points of the integrand or the end point $r = 0$.

Theorem 2 cannot help decrease the integrand in the original TDM integral since both wavefunctions are increasing in the complex plane. Therefore the second innovation of the Landau-Lifshitz approach was a transformation of the original integral into an equivalent form based on the expansion of the upper-state wavefunction into a sum of two functions, $\psi_{v'} = \psi^+_{v'} + \psi^-_{v'}$, which are also solutions of the Schrödinger equation (complex-conjugated to each other on the real axis) that are decreasing in the upper and lower half-planes, respectively. Both of them are increasing, rather than decreasing, beyond the turning points on the real axis, still the integral remains convergent because the lower-state function, $\psi_{v''}$, decays faster than $\psi^+_{v'}$ increases [4]. As a result, in the transformed integral, the integrand, 2Re $\psi_{v''} d(r) \psi^+_{v'}$, decays much more slowly over the under-barrier regions than the original integrand and therefore has reasonably small value in a vicinity of $r = 0$; in fact, this small value times the corresponding Δr is on the order of the TDM itself, which is an important feature to be used below. Note, just in case, that the technique of "fine cancellation" of two exponentially increasing functions to give a physically justified decreasing one is alien to numerical calculations.

(vii) In the transformed integral, the $\psi^+_{v'}$ function of the upper state decreases in the upper half-plane faster than the lower-state function increases. Therefore, we can shift C, while keeping its start point fixed at $r = 0$, in such a way as to decrease the integrand as much as possible in order to make the integrand on the order of the integral itself. If done successfully, the integrand first increases

from zero at $r = 0$, then reaches a maximum somewhere at path C in a vicinity of the physical Coulomb singularity, $r = 0$, and then decreases when moving away along path C. Thus, as mentioned above, the value at this maximum times the corresponding length of convergence, Δr, is the desirable TDM. In such a case, the above 5% error in the integrand will again result in a 5% relative error in the whole integral because the integrand and the integral are again of one and the same order of magnitude.

(viii) Theorem 3 implies that **analysis of singularities of the PEF and DMF becomes crucial**. There exists a single *physical* pole of the PEF at $r = 0$ due to the Coulomb nuclear repulsion that gives rise to the repulsive branch of the PEF. As was shown by one of us (see references in [4]), under the very weak restriction of the repulsive branch being exponential, the intensities of the $v-0$ ($v > 1$) vibrational overtone transitions associated with the repulsive branch of the potential obey the so-called Normal Intensity Distribution Law (NIDL), which reads that the logarithm of the intensity is linear function of the square root of the energy of the upper state in units of the vibrational quantum. Anomalies can occur at isolated transitions whose intensities drop well below the NIDL straight line.

(ix) All other singularities of the model PEF and DMF are *artificial*, i.e., they are characteristic of the model rather than the molecule. Therefore, as soon as such a singularity provides for the principal contribution to the TDM, the corresponding PEF or DMF must be rejected. In particular, the DMF should not increase or oscillate in the upper right half of the complex plane, because such behavior is definitely manifestation of a singularity either in a finite part of complex plane or at infinity. This singularity can also make shifting the integration path useless.

(x) Since the only singularity at $r = 0$ is permitted to contribute to the TDM, we come to the third key point: **The calculated intensities must follow the NIDL**.

(xii) In order to further decrease the errors, **the model functions must follow the intrinsic functions as closely as possible, including *ab initio* data points over the entire r axis and the theoretical limits of the united and separated atoms**.

Figures 1 and 4 illustrate the notions of the "correct" and "wrong" model functions: the former provide for the intensity distributions obeying the NIDL, as curves *3–5* in the Fig. 1, circles and triangles in Fig. 4; in contrast, the latter result in the wavy distributions declining from the NIDL, squares in Fig. 4.

An additional validation check can be provided based on the quasi-classical approximation to the TDM, see Ref. [4, Appendix] (paper I; we will add I to the equation numbers cited). The TDM is calculated by Eq. (IA.2),

$$\mathrm{TDM} = 2\mathrm{Re}\int_C \psi_{v''J''} d(r) \psi^+_{v'J'} dr \tag{A.1}$$

(we restore the rotational quantum numbers omitted in paper I), where the integration path C starts at $r = 0$ and goes in the upper half-plane circumventing

the turning points. The quasi-classical approximation leads to Eq. (IA.13),

$$\mathrm{TDM}_{\mathrm{qcl}} = B_0 T_0. \tag{A.2}$$

The pace of the intensity fall-off with the overtone number at $\Delta v = v' - v'' \gg 1$ is given by factor T_0^2 that depends only on the potential and can be easily calculated by the formula

$$T_0 = \exp\left(-\Delta\Phi_0\right), \tag{A.3}$$

where

$$\Delta\Phi_0 = \frac{\sqrt{2\mu}}{\hbar}\left\{\int_{r_0}^{r^-_{v''J''}} \sqrt{U_{J''}(r) - E_{v''J''}}dr - \int_{r_0}^{r^-_{v'J'}} \sqrt{U_{J'}(r) - E_{v'J'}}dr\right\}. \tag{A.4}$$

Point r_0 is chosen at the real axis deep enough in the repulsive region,

$$U_J\left(r_0\right) \gg E_{vJ}, \tag{A.5}$$

so that $\Delta\Phi_0$ is nearly independent of r_0 (see below); $r^-_{v'J'}$ and $r^-_{v''J''}$ are the left turning points at the corresponding energies. We will see that

$$B_0 = C_0/\Delta v, \tag{A.6}$$

where C_0 is on the order of 1 debye.

As seen in Fig. A.10, the quasi-classical approximation excellently reproduces the exponential fall-off of the intensity of the R(0) line with the overtone number despite the fact that factor T_0 in Eqs. (A.2)-(A.4) responsible for such behavior does not contain the DMF at all. Remarkably, the pace of the intensity fall-off, which any DMF must provide for, can be established with such a simple means. Indeed, the calculation in Eq. (A.4) is as simple as two-by-two: one needs only the potential, and only in the repulsive region, and even in an arbitrary form including a set of spline-interpolated *ab initio* points.

Finally, we derive the explicit expression for pre-factor B_0. In Eq. (A.1), path C is shifted far enough from the turning points, so that the wave functions can be replaced with their quasi-classical expressions given by Eqs. (IA.3-9). In order to simplify notations, we introduce the functions

$$\pi_{vJ}(r) \equiv -ip_{vJ}(r) = \sqrt{2\mu\left[U_J(r) - E_{vJ}\right]},$$
$$\Phi_{vJ}(r) = \hbar^{-1}\int_{r^-_{vJ}}^{r} \pi_{vJ}(r)dr.$$

The square root is defined to be positive at the real axis at $r < r^-_{vJ}$ where $U_J(r) \gg E_{vJ}$. The square roots in the denominators of Eqs. (IA.3,4) are defined this way, too. When these functions are numerically integrated in the complex plane, the code must verify the continuity of their changes between adjacent points at path C in order to avoid jumps between two branches of the

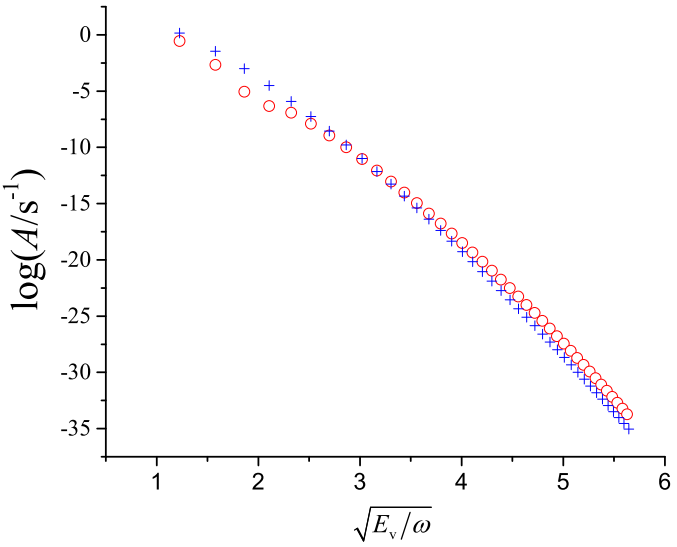

Figure A.10: Comparison of the quasi-classical approximation to the Einstein A coefficients (pluses) with the exact ones (circles). The quasi-classical TDMs for v–0 R(0) intensities were calculated by Eqs. (A.2) and (A.6) in which C_0 is put to 1 debye.

square-root functions. Inserting Eqs. (IA.3,4) into Eq. (IA.2), we obtain

$$\mathrm{TDM}_{\mathrm{qcl}} = 2A_{v'J'}A_{v''J''}\sqrt{\frac{q_{v'}}{q_{v''}}}\mathrm{Re}(-i)\int_C \frac{d(r)dr}{\sqrt{\pi_{v'J'}(r)\pi_{v''J''}(r)}}e^{-\Delta\Phi(r)}, \quad \text{(A.7)}$$

$$\Delta\Phi(r) \equiv \Phi_{v'J'}(r) - \Phi_{v''J''}(r) = \Delta\Phi_0 + \hbar^{-1}\int_{C_0}\left[\pi_{v'J'}(r) - \pi_{v''J''}(r)\right]dr, \quad \text{(A.8)}$$

where A_{vJ} and q_v are quasi-classical normalizing coefficients and harmonic corrections, respectively, explicitly given by Eqs. (IA.6-9), and $\Delta\Phi_0$ is given by Eq. (A.4); path C_0 in Eq. (A.8) starts at some real point r_0 satisfying condition (A.5) and ends at a given r belonging to path C. The choice of r_0 is arbitrary as long as condition (A.5) is fulfilled. This uncertainty reflects the fact that separation of TDM into the exponential part and the pre-factor is not unique: one can always move a part of T_0 into B_0 provided this part slowly varies with Δv. Note that path C in Eq. (A.7) can also start at r_0 because the integrand is real-valued at $0 < r < r_0$, and, in what follows, this will be implicitly assumed.

For the pre-factor, we obtain

$$B_0 = 2A_{v'J'}A_{v''J''}\sqrt{\frac{q_{v'}}{q_{v''}}}\mathrm{Im}\int_C \frac{d(r)dr}{\sqrt{\pi_{v'J'}(r)\pi_{v''J''}(r)}}e^{-\varphi(r)}, \quad \text{(A.9)}$$

$$\varphi(r) = \hbar^{-1}\int_{C_0}\left[\pi_{v'J'}(r) - \pi_{v''J''}(r)\right]dr. \quad \text{(A.10)}$$

For calculation of curve *5* in Fig. 1, path C was chosen to consist of two line segments: $r_0 + ix$ $(0 \le x \le 0.4)$ and $x + i0.4$ $(r_0 \le x < \infty)$.

In order to estimate B_0, we will calculate it for $d(r) \equiv const = \bar{d}$, where $\bar{d}$ is generally a complex number whose absolute value is on the order of the average dipole moment over C, say 1 debye; in particular, B_0 is merely the overlap integral if $const = 1$. We also will neglect the difference between J' and J''. Along path C, the potential energy is very high according to (A.5), therefore Eq. (A.10) is easily converted to

$$\varphi(r) = \frac{\Delta E\sqrt{2\mu}}{2\hbar}y(r), \quad \text{(A.11)}$$

$$y(r) = \int_{C_0}\frac{dr}{\sqrt{U_J(r)}}, \quad \text{(A.12)}$$

where $\Delta E = E_{v'J'} - E_{v''J''}$. The potential has zero at equilibrium, its phase ϕ is defined to be 0 at r_0, and ϕ decreases by 2π when r moves along C to infinity, hence $\sqrt{U_J(r)}$ becomes negative and tending to $-\sqrt{D_\mathrm{e}}$; thus, $y(r)$ vanishes at $r = r_0$ and $y(r) \to -\infty$ at the far end of C_0. Equation (A.9) transforms to the

approximate relation

$$B_0 \approx 2A_{v'J'}A_{v''J''}\sqrt{\frac{q_{v'}}{2\mu q_{v''}}}\mathrm{Im}\ \bar{d}\int_C \frac{dr}{\sqrt{U_J(r)}}\exp\left[\frac{\Delta E\sqrt{2\mu}}{2\hbar}y(r)\right]$$
$$= 2A_{v'J'}A_{v''J''}\sqrt{\frac{q_{v'}}{2\mu q_{v''}}}\mathrm{Im}\ \bar{d}\int_0^{-\infty}\exp\left[\frac{\Delta E\sqrt{2\mu}}{2\hbar}y\right]dy$$
$$= -\frac{2\hbar A_{v'J'}A_{v''J''}}{\mu\Delta E}\sqrt{\frac{q_{v'}}{q_{v''}}}\mathrm{Im}\ \bar{d}. \qquad \text{(A.13)}$$

For the overlap integral, $const = 1$, hence $B_0 = 0$, as should be for the overlap between the wave functions of the states belonging to a common potential $U_J(r)$. Substitution of the normalization constants[5] of Eqs. (IA.7,8) into Eq. (A.13) gives

$$B_0 \approx -\frac{2\hbar}{\Delta E\sqrt{t_{v'J'}t_{v''J''}}}\mathrm{Im}\ \bar{d} \propto \frac{\hbar\omega_e}{\Delta E}\mathrm{Im}\ \bar{d} \approx \frac{1}{\pi\Delta v}\mathrm{Im}\ \bar{d}, \qquad \text{(A.14)}$$

where t_{vJ} is period of vibrations and we neglected the small differences between q_v and unity. We see that Eq. (A.14) has the form of Eq. (A.6).

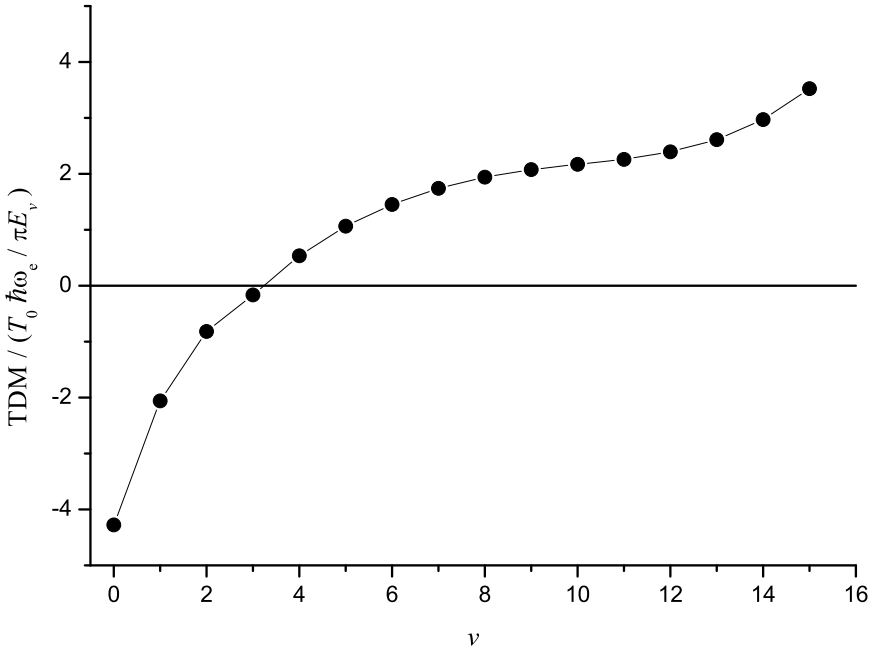

Figure A.11: The calculated values of the TDM (in debye) for the R(0) line in the v–0 bands.

[5]The signs of these constants were based on the convention that the wave functions are positive at large r. Here, the convention is changed according to footnote 4 so that factor $(-1)^v$ disappears.

The uncertainties introduced to Eq. (A.13) in the above derivation come from neglecting E_{vJ} as compared to $U_J(r)$ and the difference between J' and J'' in the integral. Omitting the energies has little impact on the integral because the potential at path C is actually much larger than the energies. The errors due to putting $J' = J'' = J$ are beyond 3-4 significant digits.

Figure A.11 demonstrates the effect of the TDM sign change at the anomaly 3-0 on condition that the signs of the wave functions were selected according to footnote 4.

References

[1] L. Yorke, S. N. Yurchenko, L. Lodi, J. Tennyson, ExoMol molecular line lists. VI. A high temperature line list for phosphorus nitride, Mon. Not. R. Astron. Soc. 445 (2014) 1383–1391. doi:10.1093/mnras/stu1854.

[2] M. Semenov, N. El-Kork, S. N. Yurchenko, J. Tennyson, Rovibronic spectroscopy of PN from first principles, PCCP 23 (2021) 22057 – 22066. doi:10.1039/d1cp02537f.

[3] E. S. Medvedev, V. G. Ushakov, Selection of the model functions for calculations of high-overtone intensities in the vibrational-rotational spectra of diatomic molecules, Opt. Spectrosc. 130 (2022) 1077–1084. doi:10.21883/EOS.2022.09.54822.3428-22.

[4] E. S. Medvedev, V. G. Ushakov, Irregular semi-empirical dipole-moment function for carbon monoxide and line lists for all its isotopologues verified for extremely high overtone transitions, J. Quant. Spectrosc. Radiat. Transfer 288 (2022) 108255. doi:10.1016/j.jqsrt.2022.108255.

[5] G. Cazzoli, L. Cludi, C. Puzzarini, Microwave spectrum of $P^{14}N$ and $P^{15}N$: Spectroscopic constants and molecular structure, J. Mol. Struct. 780-781 (2006) 260–267. doi:10.1016/j.molstruc.2005.07.010.

[6] V. V. Meshkov, A. Y. Ermilov, A. V. Stolyarov, E. S. Medvedev, V. G. Ushakov, I. E. Gordon, Semi-empirical dipole-moment function of carbon monoxide and line lists for all its isotopologues revisited, J. Quant. Spectrosc. Rad. Transfer 280 (2022) 108090. doi:10.1016/j.jqsrt.2022.108090.

[7] G. M. J. Barca, C. Bertoni, L. Carrington, D. Datta, N. De Silva, J. E. Deustua, D. G. Fedorov, J. R. Gour, A. O. Gunina, E. Guidez, T. Harville, S. Irle, J. Ivanic, K. Kowalski, S. S. Leang, H. Li, W. Li, J. J. Lutz, I. Magoulas, J. Mato, V. Mironov, H. Nakata, B. Q. Pham, P. Piecuch, D. Poole, S. R. Pruitt, A. P. Rendell, L. B. Roskop, K. Ruedenberg, T. Sattasathuchana, M. W. Schmidt, J. Shen, L. Slipchenko, M. Sosonkina, V. Sundriyal, A. Tiwari, J. L. Galvez Vallejo, B. Westheimer, M. Wloch, P. Xu, F. Zahariev, M. S. Gordon, Recent developments in the general

atomic and molecular electronic structure system, J. Chem. Phys. 152 (2020) 154102. doi:10.1063/5.0005188.

[8] H.-J. Werner, P. J. Knowles, F. R. Manby, J. A. Black, K. Doll, A. Heßelmann, D. Kats, A. Köhn, T. Korona, D. A. Kreplin, Q. Ma, T. F. MillerIII, A. Mitrushchenkov, K. A. Peterson, I. Polyak, G. Rauhut, M. Sibaev, The Molpro quantum chemistry package, J. Chem. Phys. 152 (2020) 144107. doi:10.1063/5.0005081.

[9] Z. Qin, J. M. Zhao, L. H. Liu, Energy levels, transition dipole moment, transition probabilities and radiative lifetimes for low-lying electronic states of PN, J. Quant. Spectrosc. Rad. Transfer 227 (2019) 47–56. doi:10.1016/j.jqsrt.2019.02.002.

[10] E. G. Lee, J. Y. Seto, T. Hirao, P. F. Bernath, R. J. Le Roy, FTIR emission spectra, molecular constants, and potential curve of ground state GeO, J. Mol. Spectrosc. 194 (1999) 197–202. doi:10.1006/jmsp.1998.7789.

[11] H. M. Hulburt, J. O. Hirschfelder, Potential energy functions for diatomic molecules, J. Chem. Phys. 9 (1941) 61–69. doi:10.1063/1.1750827.

[12] P. G. Hajigeorgiou, Compact and accurate models for the diatomic potential energy, Mol. Phys. 120 (2022) e2133754. doi:10.1080/00268976.2022.2133754.

[13] P. G. Hajigeorgiou, The extended Hulburt–Hirschfelder long-range oscillator model for direct-potential-fit analysis, Int. J. Quant. Chem. 118 (2017) e25498. doi:10.1002/qua.25498.

[14] J. Goodisman, Dipole-moment function for diatomic molecules, J. Chem. Phys. 38 (1963) 2597–2599. doi:10.1063/1.1733557.

[15] A. A. Radzig, B. M. Smirnov, Reference Data on Atoms, Molecules, and Ions, Vol. 31 of Springer Series in Chemical Physics, Springer, Berlin, 1985.

[16] F. C. Wyse, E. L. Manson, W. Gordy, Millimeter wave rotational spectrum and molecular constants of $^{31}P^{14}N$, J. Chem. Phys. 57 (1972) 1106–1108. doi:10.1063/1.1678365.

[17] E. S. Medvedev, V. V. Meshkov, A. V. Stolyarov, V. G. Ushakov, I. E. Gordon, Impact of the dipole-moment representation on the intensity of high overtones, J. Mol. Spectrosc. 330 (2016) 36–42. doi:10.1016/j.jms.2016.06.013.

[18] E. S. Medvedev, Towards understanding the nature of the intensities of overtone vibrational transitions, J. Chem. Phys. 137 (2012) 174307. doi:10.1063/1.4761930.

[19] A. G. Maki, F. J. Lovas, The infrared spectrum of $^{31}P^{14}N$ near 1300 cm^{-1}, J. Mol. Spectrosc. 85 (1981) 368–374. doi:10.1016/0022-2852(81)90209-5.

[20] S. N. Ghosh, R. D. Verma, J. VanderLinde, A high resolution study of $A^1\Pi$-$X^1\Sigma$ transition of the PN molecule, Canad. J. Phys. 59 (1981) 1640–1652. doi:10.1139/p81-216.

[21] I. K. Ahmad, P. A. Hamilton, The Fourier Transform Infrared Spectrum of PN, J. Mol. Spectrosc. 169 (1995) 286–291. doi:10.1006/jmsp.1995.1022.

[22] J. Raymonda, W. Klemperer, Molecular Beam Electric Resonance Spectrum of $^{31}P^{14}N$, J. Chem. Phys. 55 (1971) 232–233. doi:10.1063/1.1675513.

[23] J. Hoeft, E. Tiemann, T. Törring, Rotationsspektrum des PN, Z. Naturforsch. A 27a (1972) 703–704. doi:10.1016/0584-8539(77)80083-4.

[24] V. V. Meshkov, A. V. Stolyarov, R. J. Le Roy, Adaptive analytical mapping procedure for efficiently solving the radial Schrödinger equation, Phys. Rev. A 78 (2008) 052510. doi:10.1103/PhysRevA.78.052510.

[25] L. D. Landau, E. M. Lifshitz, Quantum Mechanics: Non-Relativistic Theory, 3rd Edition, Pergamon, Oxford, 1977.

[26] S. N. Yurchenko, L. Lodi, J. Tennyson, A. V. Stolyarov, Duo: A general program for calculating spectra of diatomic molecules, Comput. Phys. Communicat. 202 (2016) 262–275. doi:10.1016/j.cpc.2015.12.021.

[27] J. D. Brown, G. Burns, R. J. Le Roy, Improved Spectroscopic Data Synthesis for $I_2(B^3\Pi^+_{Ou})$ and Predictions of J Dependence for $B(^3\Pi^+_{Ou})$-$X(^1\Sigma^+_g)$ Intensities, Can. J. Phys. 51 (1973) 1664–1677. doi:10.1139/p73-220.

[28] R. J. Le Roy, E. R. Vrscay, Periodicity of the Oscillatory J Dependence of Diatomic Molecule Franck-Condon Factors, Can. J. Phys. 53 (1975) 1560–1572. doi:10.1139/p75-198.

[29] V. G. Ushakov, S. A. Balashev, E. S. Medvedev (unpublished).

[30] H. Abgrall, E. Roueff, F. Launay, J.-Y. Roncin, J.-L. Subtil, The Lyman and Werner Band Systems of Molecular Hydrogen, J. Mol. Spectrosc. 157 (1993) 512–523. doi:10.1006/jmsp.1993.1040.

[31] R. E. Meredith, F. G. Smith, Computation of electric dipole matrix elements for hydrogen fluoride, J. Quant. Spectrosc. Radiat. Transfer 13 (1973) 89–114. doi:10.1016/0022-4073(73)90105-2.

[32] E. Medvedev, Determination of a new molecular constant from overtone vibrational spectra, J. Mol. Spectrosc. 114 (1985) 1–12. doi:10.1016/0022-2852(85)90330-3.

[33] C.-Y. Chung, J. F. Ogilvie, Y.-P. Lee, Detection of Vibrational-Rotational Band 0-3 of $^{12}C^{16}O$ $X^1\Sigma^+$ with Cavity Ringdown Absorption near 0.96 μm, J. Phys. Chem. A 109 (2005) 7854–7858. doi:10.1021/jp052035x.

[34] K. Cashion, A method for calculating vibrational transition probabilities, J. Mol. Spectrosc. 10 (1963) 182–231. doi:10.1016/0022-2852(63)90168-1.

[35] A. Ferguson, D. Parkinson, The hydroxyl bands in the nightglow, Planet. Space Sci. 11 (1963) 149–159. doi:10.1016/0032-0633(63)90136-3.

[36] E. S. Medvedev, V. G. Ushakov, A. V. Stolyarov, I. E. Gordon, Intensity anomalies in the rotational and ro-vibrational spectra of diatomic molecules, J. Chem. Phys. 147 (2017) 164309. doi:10.1063/1.5000717.

[37] E. S. Medvedev, V. G. Ushakov, High sensitivity of the anomalies in the rotational and ro-vibrational bands of carbon monoxide to small changes in the molecular potential and dipole moment, J. Mol. Spectrosc. 349 (2018) 60–64. doi:10.1016/j.jms.2018.04.008.

[38] R. E. Pike, T. R. Geballe, M. G. Burton, A. Chrysostomou, Highly excited H_2 in Herzberg-Haro 7: Formation pumping in shocked molecular gas?, Astrophys. J. 822 (2016) 82–94. doi:10.3847/0004-637X/822/2/82.

[39] P. B. Changala, D. A. Neufeld, B. Godard, Anomalous Intensities in the Infrared Emission of CH^+ Explained by Quantum Nuclear Motion and Electric Dipole Calculations, Astrophys. J. 917 (2021) 12. doi:10.3847/1538-4357/ac05c8.

[40] A.-M. Syme, L. K. McKemmish, Full spectroscopic model and trihybrid experimental-perturbative-variational line list for CN, Mon. Not. Royal Astron. Soc. 505 (2021) 4383–4395. doi:10.1093/mnras/stab1551.